AIAA JOURNAL
Vol. 42, No. 6, June 2004

Optimal Shape Design of a Two-Dimensional Asymmetric Diffuser in Turbulent Flow

Seokhyun Lim* and Haecheon Choi†
Seoul National University, Seoul 151-744, Republic of Korea

An optimal shape of two-dimensional asymmetric diffuser with maximum pressure recovery at the exit is numerically obtained using a mathematical theory based on the variational calculus and gradient algorithm. The initial diffuser is taken to be a two-dimensional asymmetric diffuser for which much experimental and numerical data are available. The Reynolds number based on the bulk mean velocity and the channel height at the diffuser entrance is 1.8×10^4. From this initial shape, optimal diffuser shapes are designed for six different geometric constraints, such as the streamwise length and height of the diffuser. The optimality condition for maximum pressure recovery is obtained to be zero skin friction along the diffuser wall. The turbulent flow inside the diffuser is predicted using the k–ϵ–v^2–f model, and optimal shapes are obtained through iterative procedures to satisfy the optimality condition. With the shape design, flow separation that appeared in the initial diffuser is completely removed or significantly reduced. For one of the optimal diffuser shapes obtained, large-eddy simulation is carried out to validate the result of the shape design. The wall shear stress, wall pressure, mean velocity, and turbulence quantities obtained from large-eddy simulation are in good agreement with those from the simulation using the turbulence model.

I. Introduction

THE diffuser is a device that converts the kinetic energy of the flow into potential energy by broadening its height to decelerate the velocity and recover the pressure. However, when the diffuser height increases too much in the streamwise direction, flow separation occurs inside the diffuser due to the strong adverse pressure gradient formed, and consequently, the actual flow passage becomes narrow, resulting in a serious pressure loss. Therefore, flow separation is an important factor that should be considered to enhance the performance of the diffuser.

In application, straight-wall diffusers are commonly used due to their simple geometry, and many studies have been performed about the parameters that affect the performance of a two-dimensional, straight-wall diffuser.[1–4] Among them, Reneau et al.[4] provided complete performance maps of a two-dimensional, straight-wall diffuser according to geometric parameters such as the length, area ratio, and expansion angle of the diffuser and the blockage parameter of the inlet turbulent boundary-layer flow.

Studies on modifying the diffuser wall shape have been also conducted to improve the diffuser performance. In his pioneering work, Stratford[5,6] obtained theoretically a pressure distribution that maintains zero skin friction throughout the region of pressure rise inside a diffuser, and constructed experimentally a diffuser having the theoretical pressure distribution by controlling each segment of the diffuser wall. Maintaining zero skin friction along the diffuser wall suggests that the diffuser should be widened as much as possible but preventing flow separation. Hence, the diffuser designed in this way is expected to have maximum pressure recovery. The work by Stratford[5,6] has been an important motivation for many studies on turbulent boundary-layer flow in the vicinity of separation.[7–12] Carlson et al.[13] built three different two-dimensional diffusers (bell shaped, trumpet shaped and straight walls) and investigated the effect of contouring the diffuser wall shape. Their results showed that the bell-shaped walls gave slightly better pressure recovery than the straight walls in unstalled and lightly stalled diffusers, whereas the highest pressure recovery was attained with the straight walls in highly stalled diffusers. Strawn and Kline[14] designed an optimum wall shape of a diffuser using an inverse method and a prediction tool based on the momentum integral equation that is valid only for a diffuser with a thin turbulent boundary layer and irrotational potential core (also see Refs. 15 and 16). They concluded that a modest gain was achieved for short-length diffusers but there was little or no gain for long-length diffusers.

Traditionally, shape design methods have primarily relied on physical intuition. However, these methods may need much trial and error, and the shape obtained is not necessarily an optimal one. Therefore, systematic shape design methods using mathematical theories have been developed. Pironneau[17,18] suggested an optimal shape design algorithm for the first time and derived the optimality condition for a body with minimum drag in low-Reynolds-number laminar flow. An approximate shape satisfying the optimality condition suggested by Pironneau[18] was obtained by Glowinski and Pironneau[19] using the potential theory and boundary-layer integral equation. With the increase in computing power, shape optimization has now become one of the most active areas in fluid mechanics because of its wide applicability to engineering problems.

The optimal shape design algorithm based on the gradient method, that is, searching for an optimal shape by calculating the gradient of the cost function with respect to the shape change has been widely used, although it guarantees only a local optimum. The gradient of the cost function is obtained either by sensitivity analysis[20–22] or by the adjoint equation,[23–27] and the latter is more efficient than the former when the number of the design variables is large. Optimal shape design algorithms to obtain the global optimum have also been developed using genetic algorithms, response surface techniques and simulated annealing algorithms.[28–31] The main disadvantage of these methods, however, is that a great number of trials is required to obtain the optimum.

Thus far, many studies on optimal shape design using a mathematical theory have focused on low-Reynolds-number laminar flows. However, several studies have been recently conducted on the optimal shape design in turbulent flows. Zhang et al.[32] designed an optimal shape of a plane diffuser with maximum pressure recovery in turbulent flow. The optimality condition obtained by them was such that the skin friction should be zero along the diffuser wall, which coincides with the physical intuition by Stratford.[5,6] The work by Zhang et al. may be the first application of optimal shape design to fully viscous turbulent flow, although the turbulence model used

---

Received 18 June 2003; revision received 10 December 2003; accepted for publication 18 December 2003.

*Research Fellow, Center for Turbulence and Flow Control Research, Institute of Advanced Machinery and Design.

†Associate Professor, School of Mechanical and Aerospace Engineering; choi@socrates.snu.ac.kr. Senior Member AIAA.

was not so accurate in predicting separated flow. There are also other studies on the inverse design and optimal shape design of an airfoil in turbulent flow.[33–36]

In the present study, we apply an optimal shape design algorithm based on the gradient method with the adjoint equation, first proposed by Pironneau,[17,18] to a problem similar to that investigated by Zhang et al.,[32] that is, optimal shape design of a two-dimensional diffuser in turbulent flow with maximum pressure recovery at the exit. The main difference between the present study and Zhang et al. is that we use the k–ϵ–v^2–f model proposed by Durbin[37,38] for the accurate prediction of separated flow. The initial diffuser shape is set to be a two-dimensional asymmetric diffuser for which many studies have been performed.[39–41] A fully developed channel flow is provided at the diffuser inlet and the Reynolds number based on the bulk mean velocity u_b, and the channel height at the diffuser entrance, h_1, is 1.8×10^4. The results from the simulation with the k–ϵ–v^2–f turbulence model for the initial shape are compared with results available in the literature, and from this initial shape, the optimal shape of a diffuser satisfying the optimality condition for maximum pressure recovery at the exit is obtained through the iterative solutions of the Navier–Stokes equation and its adjoint equation.

In this study, we design optimal shapes for six different geometric constraints (cases 1–6) such as the length L and outlet height h_2 of the diffuser. In cases 1–3, the diffuser lengths (L/h_1) are fixed as 20, 60, and 75, respectively, and the diffuser outlet height (h_2/h_1) changes freely. In cases 4–6, the diffuser length varies as $L/h_1 = 20$, 40, and 60, respectively, at a fixed diffuser outlet height of $h_2/h_1 = 4.7$. For the optimal diffuser shape of case 5, we perform large-eddy simulation to verify the shape design result.

II. Shape Design Procedure

Figure 1 shows the schematic diagram of the initial two-dimensional asymmetric diffuser.[39–41] The heights of the diffuser entrance and exit are h_1 and h_2, respectively. The diffuser length is L, and the inlet and tail channels, whose respective lengths are L_I and L_O, are connected to the diffuser entrance and exit, respectively. Γ_I and Γ_O are the diffuser entrance and exit boundaries. Γ_M is the diffuser wall boundary to be designed, and Γ_F is the fixed diffuser wall boundary. Γ_I, Γ_M, Γ_O, and Γ_F constitute Γ; the inner domain enclosed by Γ is Ω. P_ε in Fig. 1 is determined by moving each point P on Γ_M in the outward normal direction by the magnitude of $\varepsilon\zeta(s)$, where $\zeta(s)$ is an arbitrary function of the arc length s along the wall. $\Gamma_{M,\varepsilon}$ is a new diffuser wall boundary that consists of P_ε. Here, ε is a very small positive number, and α is the opening angle of the diffuser.

Turbulent mean flow inside the diffuser satisfies the continuity and Reynolds averaged Navier–Stokes (RANS) equations and boundary conditions:

$$u_{i,i} = 0, \qquad u_j u_{i,j} = -p^*_{,i} + [(\nu + \nu_t)(u_{i,j} + u_{j,i})]_{,j} \tag{1}$$

in Ω,

$$u_1 = u_I(y), \qquad u_2 = 0$$

on Γ_I,

$$u_1 = u_O(y), \qquad u_2 = 0 \tag{2}$$

on Γ_O, and

$$u_1 = u_2 = 0$$

on Γ_M and Γ_F, where $p^* = p/\rho + (\frac{2}{3})k$. Here, u_i, ν, ν_t, p, k, and ρ are the time-averaged mean velocity, kinematic viscosity, eddy viscosity, time-averaged pressure, turbulent kinetic energy, and density, respectively. The Reynolds number is defined as $Re = u_b h_1/\nu$, where u_b is the bulk mean velocity at Γ_I.

The cost function to be maximized is defined as

$$J(\Gamma_M) = \frac{1}{u_b h_1}\left(\int_{\Gamma_I} p^* u_i n_i \,\mathrm{d}s + \int_{\Gamma_O} p^* u_i n_i \,\mathrm{d}s\right) \tag{3}$$

which is the velocity-averaged pressure recovery and is commonly used in the turbomachinery society as a performance indication of the diffuser. Also, the mathematical procedure of obtaining the optimality condition becomes much simpler with Eq. (3) than with the area-averaged pressure recovery as a cost function, that is,

$$J(\Gamma_M) = -\frac{1}{h_1}\int_{\Gamma_I} p^* \,\mathrm{d}s + \frac{1}{h_2}\int_{\Gamma_O} p^* \,\mathrm{d}s$$

Note that the first and second terms in the right-hand side of Eq. (3) are negative and positive, respectively, and increasing J is directly associated with the increase in the velocity-averaged pressure at Γ_O.

Let ϕ_i, π, and δJ be the variations of the velocity u_i, pressure p, and cost function J, respectively, due to the shape change of the diffuser wall from Γ_M to $\Gamma_{M,\varepsilon}$ (Fig. 1). Then, ϕ_i and π satisfy the following perturbed equations and boundary conditions:

$$\phi_{i,i} = 0, \qquad u_j \phi_{i,j} + \phi_j u_{i,j} = -\pi_{,i} + [(\nu + \nu_t)(\phi_{i,j} + \phi_{j,i})]_{,j} \tag{4}$$

in Ω,

$$\phi_i = 0 \tag{5}$$

on $\Gamma - \Gamma_M$, and

$$\phi_i = -\zeta \frac{\partial u_i}{\partial n}$$

on Γ_M. The variation of the cost function δJ can be expressed as

$$\delta J \cdot (u_b h_1) = \oint \pi u_i n_i \,\mathrm{d}s + \iint r \phi_{i,i} \,\mathrm{d}A + \iint z_i\{[(\nu + \nu_t)(\phi_{i,j} + \phi_{j,i})]_{,j} - u_j \phi_{i,j} - \phi_j u_{i,j} - \pi_{,i}\}\,\mathrm{d}A \tag{6}$$

where z_i and r are the adjoint velocity and pressure that satisfy the following adjoint equations and boundary condition:

$$z_{i,i} = 0, \qquad [(\nu + \nu_t)(z_{i,j} + z_{j,i})]_{,j} + u_j(z_{i,j} + z_{j,i}) - r_{,i} = 0 \tag{7}$$

in Ω and

$$z_i = u_i \tag{8}$$

on Γ. Then δJ is reduced to

$$\delta J = \frac{\nu}{u_b h_1}\int_{\Gamma_M} \zeta \frac{\partial u_i}{\partial n}\frac{\partial z_i}{\partial n}\,\mathrm{d}s \tag{9}$$

In this derivation, the variation of the outflow condition due to the shape change is neglected. If not, the optimality condition can hardly be obtained.[23,32] The variation of the eddy viscosity due to the shape change is also neglected, which is frequently assumed in the derivation of the optimality condition in turbulent flow,[32,33,35] although a few studies have begun to consider the variation of the eddy viscosity toward the design of optimal shape.[36,42] Without this assumption, two to four more adjoint equations depending on the turbulence

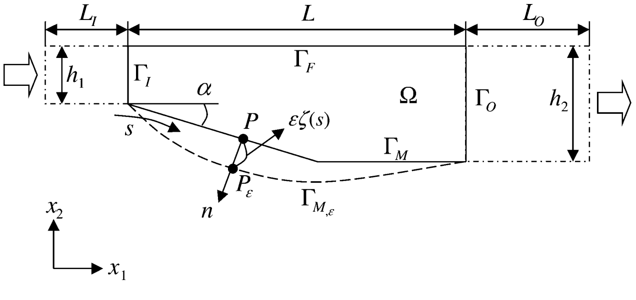

Fig. 1 Schematic diagram of a diffuser.

model should be solved to obtain the gradient of the cost function, which requires much more computational resources. Note that Zhang et al.[32] and the present study (discussed later) obtain the optimality condition of zero skin friction on Γ_M for maximum pressure recovery with this assumption, which coincides with the physical intuition by Stratford.[5,6]

With the choice of ζ in Eq. (9) as

$$\zeta(s) = \omega(s)\frac{\partial u_i}{\partial n}\bigg/\frac{\partial z_i}{\partial n} \tag{10}$$

the variation of the cost function δJ is always positive, guaranteeing that the cost function J always increases with each shape change, where $\omega(s)$ is a nonnegative weighting function of s. It is clear from Eqs. (9) and (10) that the optimality condition for maximum cost function is

$$\frac{\partial u_i}{\partial n} = 0 \tag{11}$$

on Γ_M, that is, zero skin friction on the diffuser wall, Γ_M.

The optimal shape design procedure of a diffuser with maximum pressure recovery at the exit is as follows:

1) Assume an initial diffuser shape.

2) Generate a grid inside the diffuser automatically.

3) Solve flow equations (1) and the boundary conditions (2) for u_i and p^*.

4) Solve adjoint equations (7) and boundary conditions (8) for z_i and r.

5) Obtain a new diffuser shape by moving each point on Γ_M in the outward normal direction n_i by the magnitude of $\varepsilon\zeta(s)$ in Eq. (10).

6) Iterate steps 2–5 until the cost function converges.

In the present study, the weighting function $\omega(s)$ is set to be a linear function and a sine function with a half-period, respectively, for the cases of fixing the diffuser length and fixing the diffuser outlet height, such that the magnitude of the shape change is zero at the fixed end points. We tested two different profiles of $\omega(s)$ (linear function and sine function with a quarter-period) for case 3 and obtained nearly the same optimal shapes, indicating that the shape design result is not much affected by the choice of $\omega(s)$, at least for the present problem. Also, ε is adjusted such that the magnitude of maximum shape change does not exceed 2% of the diffuser outlet height. The convergence criterion is selected such that the increase in the cost function during the last 10 iterations is less than 0.5% of the total increase.

III. Turbulence Model and Numerical Details

Flow separation is an important factor that affects the performance of a diffuser, and thus, it is important to predict accurately the separated flow characteristics during the optimal shape design of a diffuser. Therefore, in this study, we use the k–ϵ–v^2–f turbulence model (called V2F hereinafter) that has been successfully tested for separated flows.[38] According to Reneau et al.,[4] the optimum diffuser performance is achieved in the transitory stall regime. In this regime, the flow inside the diffuser is intermittently stalled. Therefore, there is a concern whether or not a steady Reynolds averaged Navier–Stokes (RANS) simulation is capable of making reliable predictions for this highly unsteady flow regime. In the present study, we consider an optimal shape design of an asymmetric diffuser as shown in Fig. 2. In this diffuser, stalls build up on the diverging wall and are washed out repeatedly with a long period of about $50h_1/u_b$ (Ref. 41), but the time-averaged mean properties have been successfully predicted by a steady RANS simulation with the V2F model.[38] Therefore, steady RANS simulations are conducted for the optimal shape design, which significantly reduces the computational resources as compared with unsteady RANS simulations.

The eddy viscosity in Eqs. (1) and (7) is determined from the V2F model as follows[38]:

$$\nu_t = C_\mu \overline{v^2} T \tag{12}$$

where $\overline{v^2}$ is the mean square of the wall-normal (or, interpreted as normal to local streamlines in a complex geometry[38]) velocity fluctuations, T is the timescale such that

$$T = \max\left[k/\epsilon,\, 6(\nu/\epsilon)^{\frac{1}{2}}\right] \tag{13}$$

where k is the turbulent kinetic energy and ϵ is the dissipation rate. To evaluate the eddy viscosity in Eq. (12), the $\overline{v^2}$ equation should be solved in addition to the k and ϵ equations, and the terms related to the pressure–velocity correlation and anisotropic dissipation in the $\overline{v^2}$ equation are modeled by a new variable f. Therefore, the final turbulence model equations to be solved are the following:

$$\begin{aligned} \rho u_j k_{,j} &= \wp - \epsilon + [(\mu + \mu_t/\sigma_k)k_{,j}]_{,j} \\ \rho u_j \epsilon_{,j} &= \left(C_{\epsilon_1}\wp - C_{\epsilon_2}\epsilon\right)\big/T + [(\mu + \mu_t/\sigma_\epsilon)\epsilon_{,j}]_{,j} \\ \rho u_j \overline{v^2}_{,j} &= kf - \overline{v^2}(\epsilon/k) + \left[(\mu + \mu_t/\sigma_k)\overline{v^2}_{,j}\right]_{,j} \\ \mathcal{L}^2 f_{,jj} - f &= (1 - C_1)\left(\left[\tfrac{2}{3} - \overline{v^2}/k\right]\big/T\right) - C_2(\wp/k) \end{aligned} \tag{14}$$

where $\wp = \mu_t(u_{i,j} + u_{j,i})u_{j,i}$ is the production term, $\mu_t = \rho\nu_t$, $\mu = \rho\nu$, σ_k, σ_ϵ, $C_{\epsilon 1}$, $C_{\epsilon 2}$, C_1, and C_2 are the model constants, and $\mathcal{L}$ is the length scale defined as

$$\mathcal{L} = C_L \ell, \qquad \ell^2 = \max\left[k^3/\epsilon^2,\, C_\eta^2(\nu^3/\epsilon)^{\frac{1}{2}}\right] \tag{15}$$

Because the four Eqs. (14) are closely correlated among themselves, two coupled sets of k–ϵ and $\overline{v^2}$–f equations are solved simultaneously as suggested by Durbin.[38] The wall boundary conditions of the turbulence variables are

$$\begin{aligned} k &= 0, & \epsilon &\to 2\nu(k/d^2) \\ \overline{v^2} &= 0, & f &\to -20\nu^2\overline{v^2}/\epsilon d^4 \end{aligned} \tag{16}$$

where d is the wall-normal distance from the wall. The model constants in Eqs. (12), (14), and (15) are

$$\begin{gathered} C_\mu = 0.19, \qquad C_{\epsilon_1} = 1.3 + \frac{0.25}{[1 + (d/2\ell)^8]}, \qquad C_{\epsilon_2} = 1.9 \\ C_1 = 1.4, \qquad C_2 = 0.3, \qquad C_L = 0.3, \qquad C_\eta = 70 \\ \sigma_k = 1, \qquad \sigma_\epsilon = 1.3 \end{gathered} \tag{17}$$

The convective terms in Eqs. (1), (7), and (14) are discretized using the third-order QUICK scheme,[43] and the pressure–velocity coupling in Eq. (1) is handled with the SIMPLER algorithm.[44]

Figure 2 shows the computational domain and grid system for the initial diffuser shape, for which many studies have been performed.[39–41] The upper boundary is the flat-plate wall and the lower boundary is the diverging wall with an opening angle α of about 10 deg. Long inlet and tail channels are connected to the diffuser entrance and exit, respectively. Nonuniform grids of 190 × 70 are used in the streamwise and wall-normal directions, respectively. The Reynolds number based on the bulk mean velocity and channel height at the inlet is $Re = u_b h_1/\nu = 1.8 \times 10^4$.

In solving the RANS equations (1) and (14), a fully developed turbulent channel flow is provided at the inlet, and the Neumann

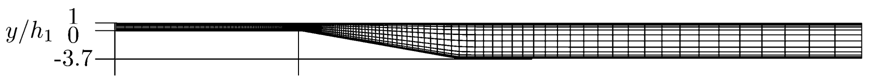

Fig. 2 Computational domain for initial diffuser, every fifth grid in the wall-normal direction shown.

boundary condition at the outlet of the tail channel, $\partial(\cdot)/\partial x = 0$, is used. Note that in Sec. II we used a Dirichlet boundary condition even at the diffuser exit for mathematical simplicity when optimality condition (11) was derived. However, the velocity profile at the exit cannot be predetermined as the shape evolves. Therefore, instead of using the Dirichlet condition at the exit, a long tail channel is introduced at the diffuser exit, and the Neumann condition is used at the outlet of the tail channel. Neglecting the variation of the outflow condition in deriving the optimality condition has a negligible effect on the result of shape design.[23,32]

The adjoint equations and the boundary condition for the adjoint velocity and pressure were given in Eq. (7) and condition (8). As shown by Cabuk and Modi,[23] the adjoint variables can be regarded as having the properties of flowing opposite to the real flow. On this account, although the adjoint variables were set to be equal to the flow variables on the boundaries in deriving the optimality condition [see condition (8)], the Neumann condition at the diffuser inlet, no-slip on the wall, and Dirichlet condition at the diffuser exit, which are the opposite to the boundary conditions of the flow variables, are imposed for the actual simulation of the adjoint equations. The same treatment of the adjoint boundary conditions was conducted by Cabuk and Modi.[23] For the stable calculation of the adjoint equation, a long inlet channel is introduced ranging from $x/h_1 = 0$ to $x/h_1 = -25$.

In practical applications, the diffuser has geometrical constraints such as the diffuser length, expansion ratio, diffuser outlet height, etc., depending on where it is used. In the present study, two different constraints are imposed: fixing the diffuser length L and fixing the diffuser outlet height h_2. In cases 1–3, the diffuser lengths (L/h_1) are fixed as 20, 60, and 75, respectively, and the diffuser outlet height (h_2/h_1) changes freely. A tail channel is connected to the end of the diffuser. In cases 4–6, the diffuser outlet height (h_2/h_1) is fixed as 4.7, which is the same as that of the initial diffuser, with varying the diffuser length (L/h_1) as 20, 40, and 60, respectively. The diffuser length, diffuser outlet height, number of grid points, and size of the computational domain for the six cases are given in Table 1. We performed grid resolution tests for the optimal diffuser shapes of cases 3 and 5, by doubling the number of grid points in both the streamwise and wall-normal directions, resulting in nearly no change in the results, for example, the changes in the pressure recovery coefficient ΔC_p, diffuser effectiveness η, and total pressure coefficient K were less than 1%, and the optimal diffuser shapes

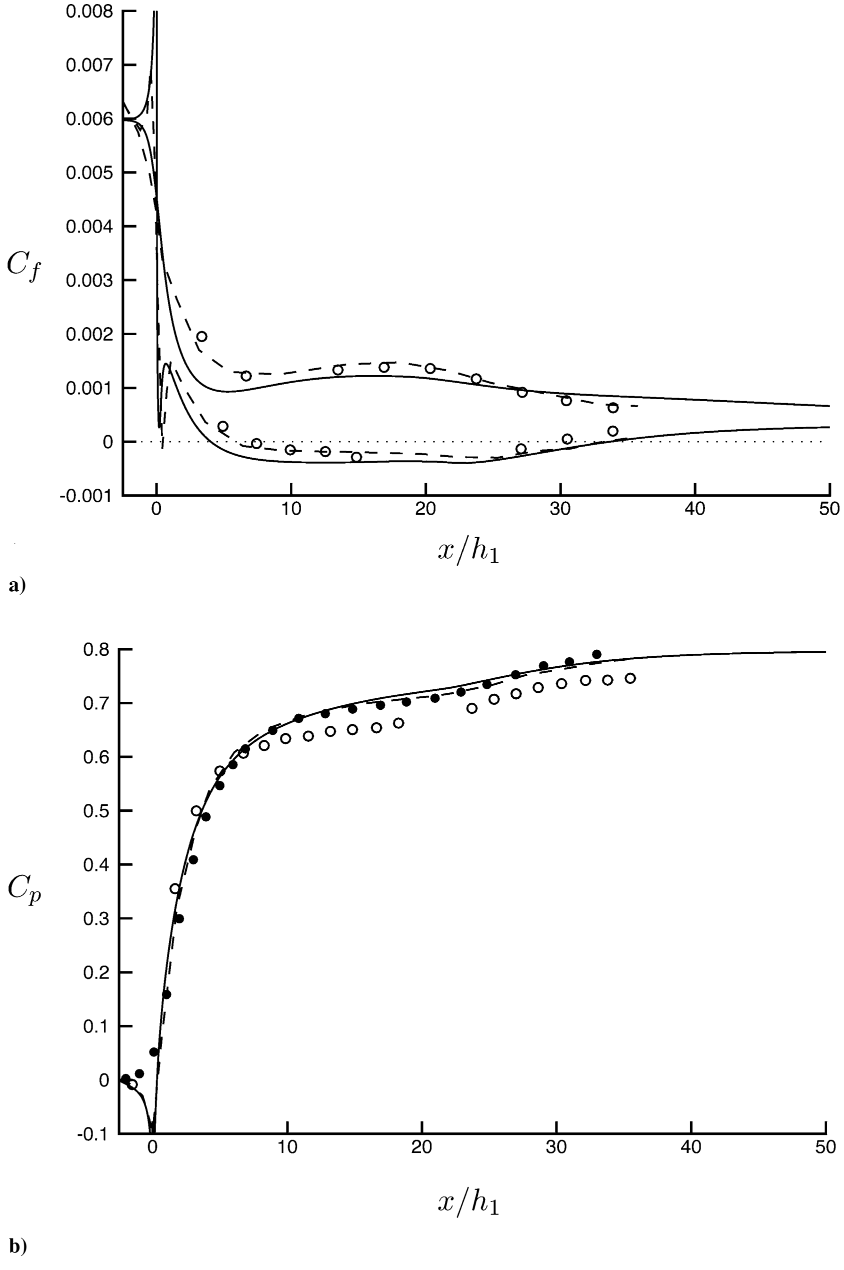

Fig. 3 Coefficients: a) skin friction coefficient along the lower and upper walls and b) pressure coefficient along the lower wall: ——, present; – – –, Kaltenbach et al.[41]; ●, Obi et al.[39]; and ○, Buice and Eaton.[40]

Table 1 Shape design cases

Case	Diffuser shape (L/h_1:h_2/h_1)	Number of grid points	Computational domain size (x/h_1)
		Fixed L	
1	20:free	220×70	$-25 \sim 100$
2	60:free	220×70	$-25 \sim 100$
3	75:free	220×70	$-25 \sim 100$
		Fixed h_2	
4	20:4.7	190×70	$-25 \sim 75$
5	40:4.7	190×70	$-25 \sim 75$
6	60:4.7	190×70	$-25 \sim 75$

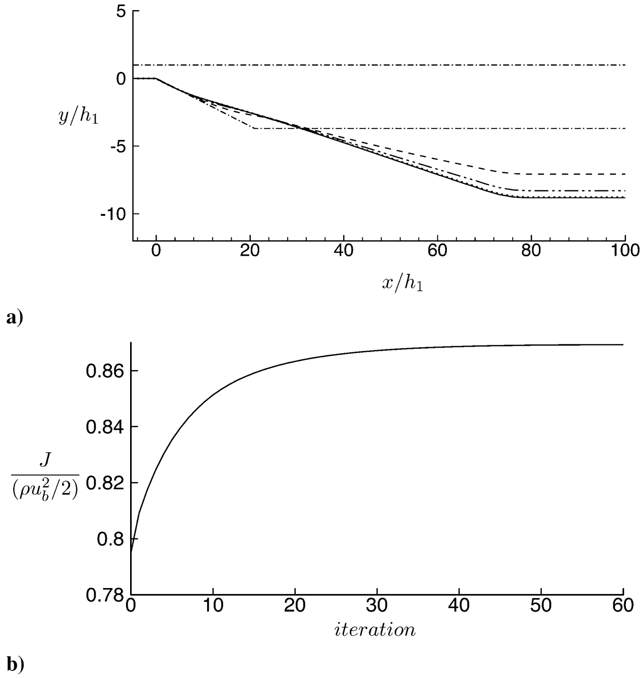

Fig. 4 Case 3: a) shape evolution at successive iterations: iteration = −·−·−, 0; – – –, 10; −··−··−, 20; · · · ·, 40; and ——, 60; and b) history of the cost function normalized by u_b.

obtained from finer resolutions were essentially the same as those from the resolutions shown in Table 1.

IV. Results of the Shape Design

Durbin[38] tested his V2F model for the initial diffuser shape (Fig. 2) and showed good agreement with the previous results for the mean velocity and turbulent kinetic energy inside the diffuser. Because the skin friction and wall pressure are important quantities in the procedure of shape design, we compare these variables predicted from the V2F model with those from previous experiments[39,40] and large-eddy simulation[41] (Fig. 3). As shown, C_f is slightly underpredicted as compared to the previous results, and the separation region ($C_f < 0$) from the present simulation is slightly larger than the previous ones.[40,41] However, the difference in C_f is tolerable, and thus, the present data can be considered reasonably good. For the wall pressure, the agreement with the existing data is excellent. Because the turbulence model used accurately predicts flow inside the diffuser, we design the optimal shape diffuser with maximum pressure recovery from this initial shape.

Next, we show the results from optimal shape design for six cases described in Table 1. First, the results from cases 1–3 are given, and then those from cases 4–6 are described.

Figure 4a shows the shape evolution from the initial shape to the optimal shape at successive iterations for case 3. At the iteration number of 40, the diffuser shape converges to the optimal shape. Here, a third-order polynomial is used to smooth out a sudden geometric variation at $x = 0$ and $x = L(= 75h_1)$, for example, around the diffuser throat, this third-order polynomial is applied in $-0.5h_1 < x < 0.5h_1$, and the radius of curvature at the throat is obtained to be about $4h_1$ throughout the iterations. Figure 4b shows the history of the cost function at successive iterations. Here, the integrations in Eq. (3) are conducted at $x/h_1 = -2.5$ for Γ_I and $x = L$ for Γ_O, respectively. A rapid increase in the cost function occurs at the first 20 iterations, and then the cost function increases slowly and converges to the optimal value.

Figure 5 shows the optimal shapes of cases 1–3 as compared with the initial shape. In all three cases, the upstream parts of the optimal diffusers are nearly identical irrespective of different geometric constraints, and they seem to be little affected by the downstream geometry (Fig. 5b). The shape of the optimal diffuser is concave up to about $x/h_1 = 10$ with an abrupt expansion around the diffuser throat and is nearly linear down to the diffuser exit, $x = L$, where a tail channel is connected. The angle of the wall section with the linear shape with respect to the streamwise x direction is about 6.2 deg, whereas the opening angle of the initial diffuser is about 10 deg.

Figure 6 shows the distribution of the skin-friction coefficient along the lower wall. In the optimal shapes, the skin frictions are zero in most of the shape design region. Because of the abrupt change in the geometry, the skin frictions near the diffuser throat are not zero even in the optimal shapes. Figure 7 shows the streamlines inside the initial and optimal diffusers (case 3). There is a wide flow-separation

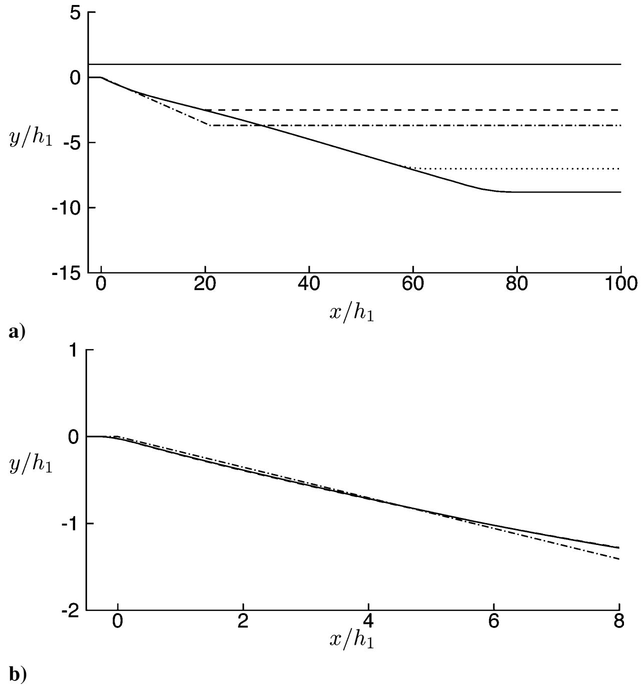

Fig. 5 Optimal shapes for different constraints: −·−·−, initial shape; optimal shape for – – –, case 1; · · · ·, case 2; and ——, case 3: a) $-2.5 \le x/h_1 \le 100$ and b) $-0.5 \le x/h_1 \le 8$.

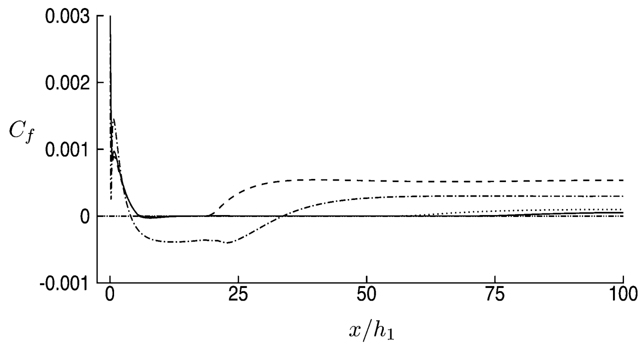

Fig. 6 Distribution of the skin-friction coefficient along the lower wall: −·−·−, initial shape; optimal shape for – – –, case 1; · · · ·, case 2; and ——, case 3.

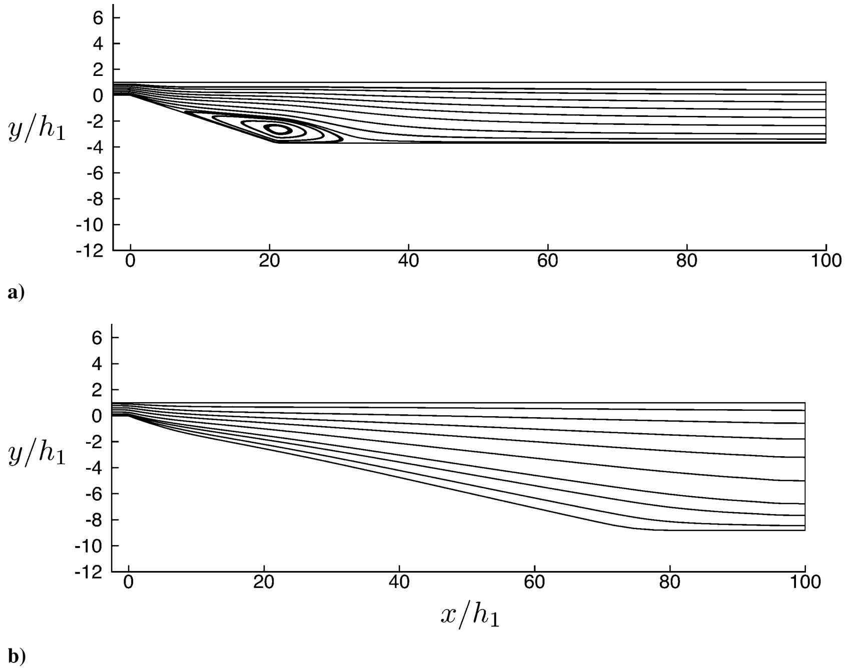

Fig. 7 Streamlines inside the diffusers: a) initial shape and b) optimal shape, case 3.

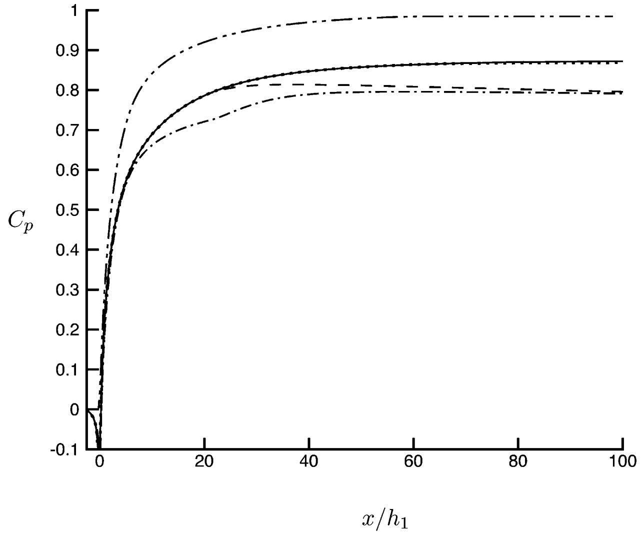

Fig. 8 Pressure distribution along the lower wall: —·—·—, initial shape; optimal shape for – – –, case 1; · · · ·, case 2; and ——, case 3; and —··—··—, ideal pressure recovery for case 2.

region in the initial shape, but flow separation is completely removed in the optimal shape. (Separation also disappears in the optimal shapes for cases 1 and 2.)

Figure 8 shows the pressure distributions along the lower wall of the initial and optimal diffusers, together with the ideal pressure recovery distribution $C_{pi}(x) = 1 - [h_1/h(x)]^2$ for case 2. As a result of removing the flow separation, a higher pressure at the diffuser exit is obtained in the optimal shape. When the diffuser length is limited to $L = 20h_1$ (case 1), the pressure rises up to $x/h_1 \simeq 20$ and remains nearly constant in the downstream, where flow enters the tail channel connected to the end of the diffuser. In spite of the smaller diffuser height [where $h_2/h_1 = 3.4$ for the optimal diffuser of case 1, but $h_2/h_1 = 4.7$ for the initial diffuser (Fig. 5a)], the pressure at $x/h_1 = 20$ in the optimal diffuser is much higher than that of the initial diffuser. The values of pressure at the exit of the tail channel are nearly the same for both the initial and optimal diffusers, but the pressure reaches this value within a shorter diffuser length in the optimal shape. In cases 2 and 3, the pressure rapidly increases up to $x/h_1 = 20 \sim 30$ and then increases very slowly in the downstream. The pressure recovery in the optimal diffuser for case 2 is nearly the same as that for case 3, which indicates that a further increase in the diffuser length [or height (Fig. 5a)] than that of case 2 is not beneficial in terms of the pressure recovery. The difference between the pressure recovery in the optimal diffuser and the ideal pressure recovery for case 2 is rather large, which is mainly due to nonzero skin friction on the upper flat wall.

Figure 9 shows the optimal shapes for cases 4–6 (the cases of fixed h_2), together with that for case 3. Note that, in cases 4–6, the diffuser outlet height is fixed to $h_2/h_1 = 4.7$, but the diffuser length changes

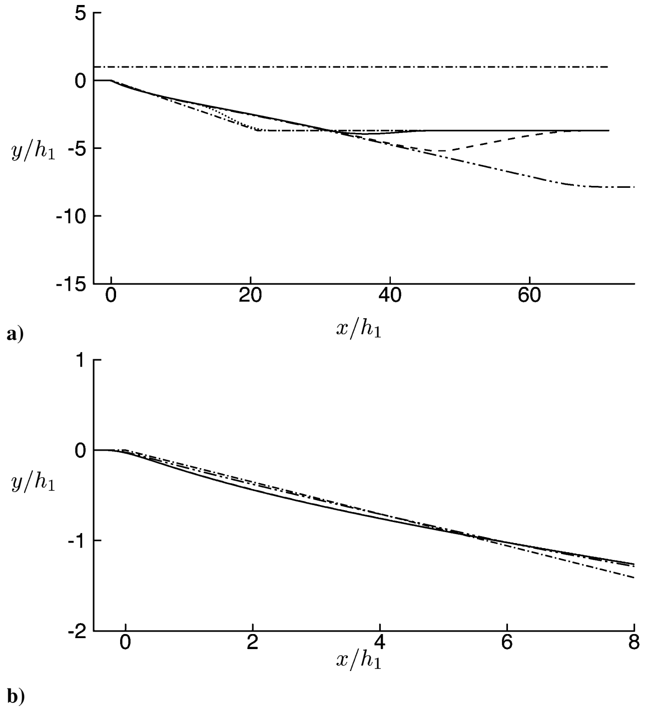

Fig. 9 Optimal shapes for different constraints: —·—·—, initial shape; optimal shape for —··—··—, case 3; · · · ·, case 4; ——, case 5; and – – –, case 6: a) $-2.5 \le x/h_1 \le 75$ and b) $-0.5 \le x/h_1 \le 8$.

as $L/h_1 = 20$, 40, and 60, respectively. The shape design region does not exactly end at $x = L$ because of the use of a third-order polynomial to smooth out a sudden geometric variation at $x = L$, as described earlier. The upstream parts of the optimal diffusers, where C_f is zero, are nearly identical regardless of the geometric constraint. However, the downstream parts, $C_f \neq 0$, are very different among themselves due to fixed h_2 (Fig. 10). Interestingly, the optimal shape of case 6 expands in height following the shape of case 3 and then contracts to satisfy the geometric constraint of fixed h_2 at the diffuser exit because of the favorable effect of keeping zero skin friction over a larger portion of the diffuser wall.

Figure 10 shows the distributions of the skin-friction coefficient along the lower walls of the initial and optimal diffusers for cases 4–6. In case 4, $L/h_1 = 20$ and $h_2/h_1 = 4.7$. Because of this severe constraint, flow separation is not removed in the optimal shape. In cases 5 and 6, the skin frictions are nearly zero in the shape design regions except near the diffuser throat and end. Figure 11 shows the streamlines inside the optimal diffusers (cases 4–6). As expected, there is no separation for cases 5 and 6, whereas a separation region exists for case 4, but the size is smaller than that in the initial diffuser (Fig. 7a).

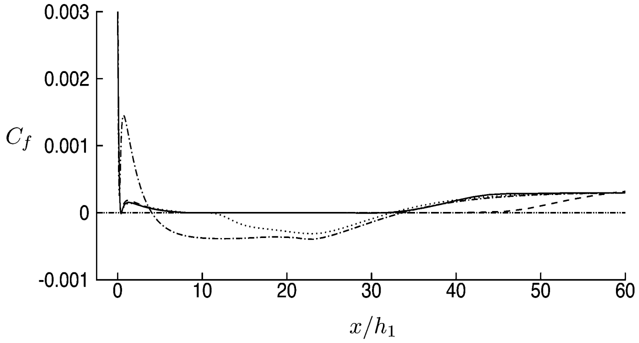

Fig. 10 Distribution of the skin-friction coefficient along the lower wall: —·—·—, initial shape; optimal shape for · · · ·, case 4; ——, case 5; and – – –, case 6.

Figure 12 shows the pressure distributions along the lower walls of the initial and optimal diffusers, together with the ideal pressure recovery distribution for case 5. In all three cases, the optimal shapes have higher pressures at the exits of the tail channels than that of the initial shape. The pressure at the exit of the tail channel in case 4 is lower than those in cases 5 and 6 because separation is not removed. Although the shape design region is extended to $L/h_1 = 60$ for case 6, the exit pressures for cases 5 and 6 are nearly the same, which indicates that, given $h_2/h_1 = 4.7$, a further increase in the diffuser length than that of case 5 is not necessary in terms of the pressure recovery. Note also that the difference between the pressure recovery in the optimal diffuser and the ideal pressure recovery for case 5 is rather large, which is mainly due to nonzero skin friction on the upper flat wall.

In the present study, the optimal shapes are obtained for maximum pressure recovery at the exit. It may be interesting to evaluate other parameters indicating the performance of a diffuser. The pressure recovery coefficients ΔC_p, diffuser effectivenesses η, and total pressure loss coefficients K of the initial and optimal shapes are shown in Table 2. These parameters are defined as[45]

$$\Delta C_p = \frac{\overline{(p)}_2 - \overline{(p)}_1}{\overline{(p_0)}_1 - \overline{(p)}_1}, \qquad \eta = \frac{\Delta C_p}{\Delta C_{pi}}, \qquad K = \frac{\overline{(p_0)}_1 - \overline{(p_0)}_2}{\overline{(p_0)}_1 - \overline{(p)}_1} \tag{18}$$

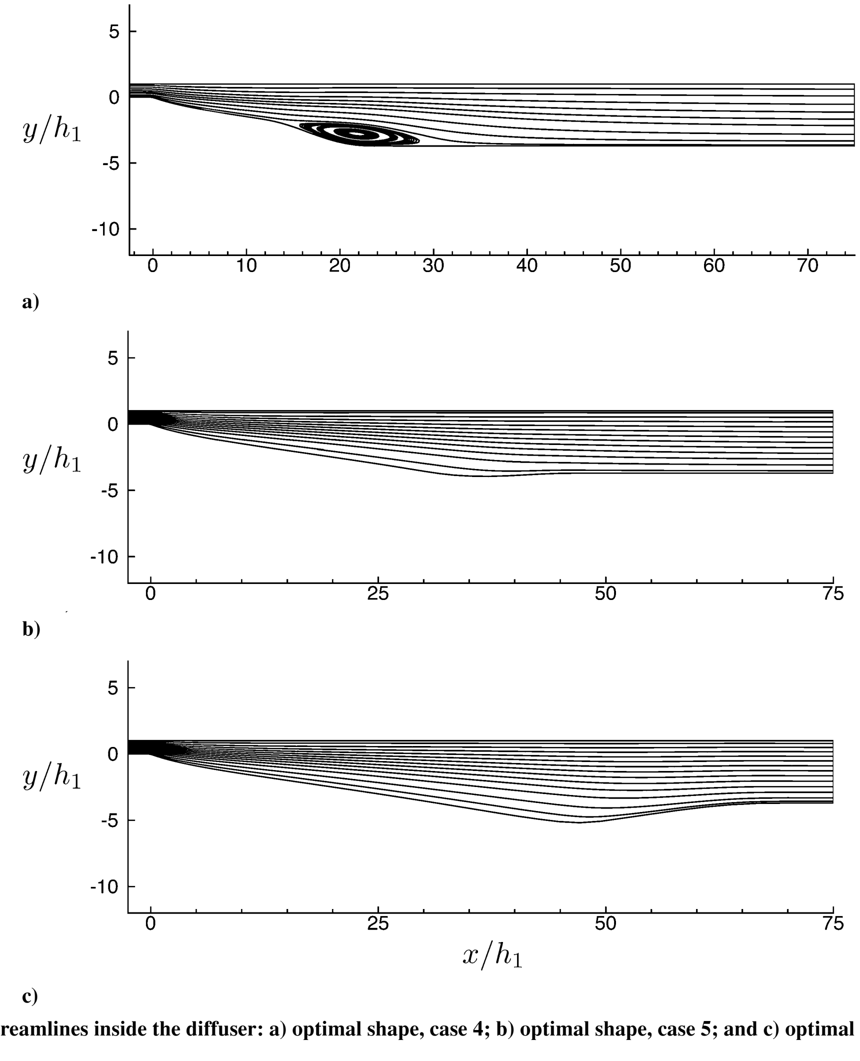

Fig. 11 Streamlines inside the diffuser: a) optimal shape, case 4; b) optimal shape, case 5; and c) optimal shape, case 6.

where $p_0 = p + \frac{1}{2}\rho V^2$ is the total pressure, $\overline{(\,)}$ indicates the velocity-averaged value across the diffuser as was done in Eq. (3), and ΔC_{pi} is the ideal pressure recovery coefficient, that is, $\Delta C_{pi} = 1 - (h_1/h_2)^2$. Here, the integrations for $(\,)_1$ and $(\,)_2$ are conducted at $x/h_1 = -2.5$ and 75, respectively. As shown in Table 2, the diffuser effectiveness is much improved and the total pressure loss is much reduced in the optimal diffusers as compared with those in the initial diffuser. The maximum increase of about 9% in the pressure recovery coefficient is obtained in the optimal diffusers for cases 2 and 3.

Figure 13 shows the distributions of the skin-friction coefficient along the lower and upper walls and the velocity profiles for the initial and optimal diffusers (case 5), to demonstrate the influence of the modification of the lower wall shape on the flow near the upper wall. As a result of the shape design, the skin friction becomes zero along the lower wall and decreases along the upper wall because of the elimination of flow separation existing in the initial diffuser. Also, in the initial shape, the flow is bent toward the upper wall due to the separation, causing high skin friction on the upper wall. The removal of flow separation in the optimal diffuser clearly reduces the distortion of the velocity profiles toward the upper wall and decreases the skin friction there. As mentioned earlier, however, the pressure in the optimal diffuser does not recover up to the ideal pressure due to the finite value of skin friction on the upper wall (Fig. 12).

Finally, it should be interesting to see whether the optimal diffuser obtained in this study shows a good performance at a different working condition, for example, at a different Reynolds number. In laminar flow, there is a significant dependence of the optimal shape on the Reynolds number.[23] However, at intermediate and high Reynolds numbers, the diffuser performance is not severely affected by the Reynolds number.[4,45,46] We have also designed the optimal shapes for case 3 at two different Reynolds numbers of 9×10^3 and 3.6×10^4 and obtained nearly the same diffuser shapes as that at $Re = 1.8 \times 10^4$, which indicates that the optimal shape obtained in this study is not very sensitive to the Reynolds number, at least in the present Reynolds number range.

Table 2 Pressure recovery coefficients ΔC_p, diffuser effectivenesses η, and total pressure loss coefficients K of the initial and optimal diffusers

	ΔC_p		η (%)		K	
Case	Initial	Optimal	Initial	Optimal	Initial	Optimal
			Fixed L			
1	0.810	0.820	84.9	89.3	0.200	0.157
2	0.810	0.884	84.9	89.7	0.200	0.158
3	0.810	0.885	84.9	89.5	0.200	0.158
			Fixed h_2			
4	0.810	0.837	84.9	87.7	0.200	0.176
5	0.810	0.854	84.9	89.4	0.200	0.160
6	0.810	0.852	84.9	89.3	0.200	0.161

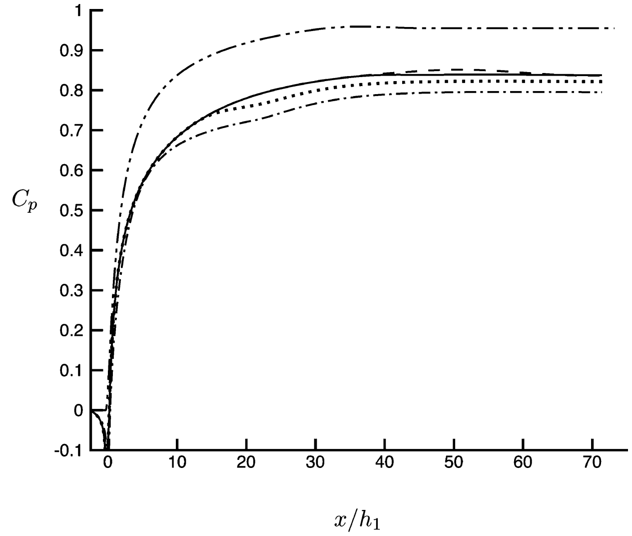

Fig. 12 Pressure distribution along the lower wall: —·—·—, initial shape; optimal shape for · · · ·, case 4; ——, case 5; and – – –, case 6; and —··—··—, ideal pressure recovery for case 5.

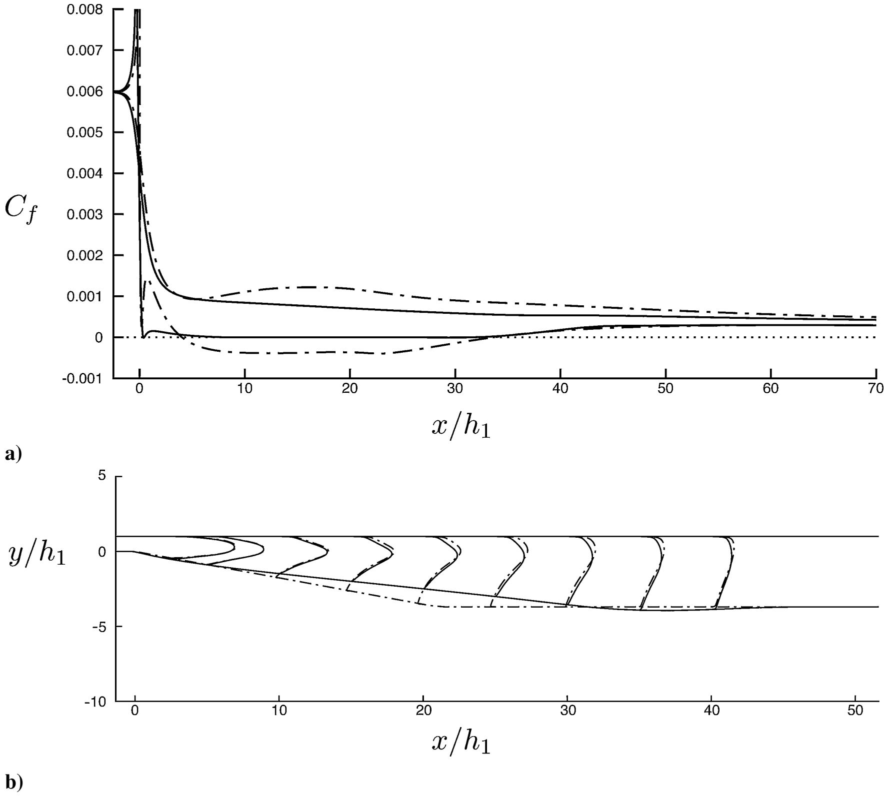

Fig. 13 Case 5: a) skin friction coefficients along the lower and upper walls and b) velocity profiles at different *x* locations: —·—·—, initial shape and ——, optimal shape.

V. Large-Eddy Simulation of Flow Inside the Optimal Diffuser

In the preceding section, we obtained the optimal diffuser shapes for six different geometric constraints using the optimal shape design method and V2F model. In this section, we perform a large eddy simulation (LES) of turbulent flow inside the optimal diffuser of case 5, which produced a maximum pressure recovery in a relatively short diffuser length ($L/h_1 = 40$) with a given diffuser outlet height ($h_2/h_1 = 4.7$), to confirm the shape design result from the V2F model.

A. Numerical Details

In our LES, we use the dynamic subgrid-scale model using the least-square method.[47,48] When the model constant is calculated, the test filter is applied in the streamwise and spanwise directions using the trapezoidal rule, and the test-to-grid filter ratio is $\hat{\Delta}/\Delta = \sqrt{6}$ (Ref. 49). For time integration, the Crank–Nicolson method is used for the viscous terms in the wall-normal direction and a third-order Runge–Kutta method for the other terms. For the spatial discretization, the second-order central difference scheme is used for the streamwise and wall-normal directions and a spectral method for the spanwise direction. All of the numerical schemes are the same as that used by Kaltenbach et al.[41]

The geometry of the optimal diffuser of case 5 is such that the diffuser exit height h_2 is $4.7h_1$ and the diffuser length L is about $40h_1$ (Fig. 9). The computational domain used is $x/h_1 = -2.5 \sim 50$ in the streamwise direction with the inlet channel of length $2.5h_1$ and the tail channel of length $10h_1$. The spanwise width is $z = 4h_1$. The numbers of grid points are $376 \times 64 \times 128$ in the streamwise, wall-normal, and spanwise directions, respectively. The computational domain size and grid resolution are determined based on the work of Kaltenbach et al.,[41] who successfully conducted LES for the initial diffuser shape, for example, at the first grid points from the upper wall, $\Delta x/h_1 = 0.085 \sim 0.3$, $\Delta y/h_1 = 0.0015 \sim 0.0027$, and $\Delta z/h_1 = 0.0315$ in $5 \le x/h_1 \le 25$ (corresponding to $\Delta x^+ = 35 \sim 85.2$, $\Delta y^+ \simeq 1$, and $\Delta z^+ = 9.2 \sim 13.7$ in wall units based on the local wall shear velocity on the upper wall).

A convective boundary condition is imposed at the exit of the tail channel and the periodic boundary condition is used in the spanwise direction. At the inlet of the computational domain, $x = -2.5h_1$, a fully developed turbulent channel flow at $Re = u_b h_1/\nu = 1.8 \times 10^4$ ($Re_\tau = u_\tau \delta/\nu = 500$) is provided from a separate LES, where u_τ is the wall shear velocity and δ ($= h_1/2$) is the channel half-height. The computational domain size for the channel inflow simulation is $5h_1$, h_1, and $4h_1$ in the streamwise, wall-normal, and spanwise directions, respectively, and the numbers of grid points are $160 \times 64 \times 128$ ($\Delta x^+ = 30$, $\Delta y^+ = 1 \sim 40$, and $\Delta z^+ = 30$).

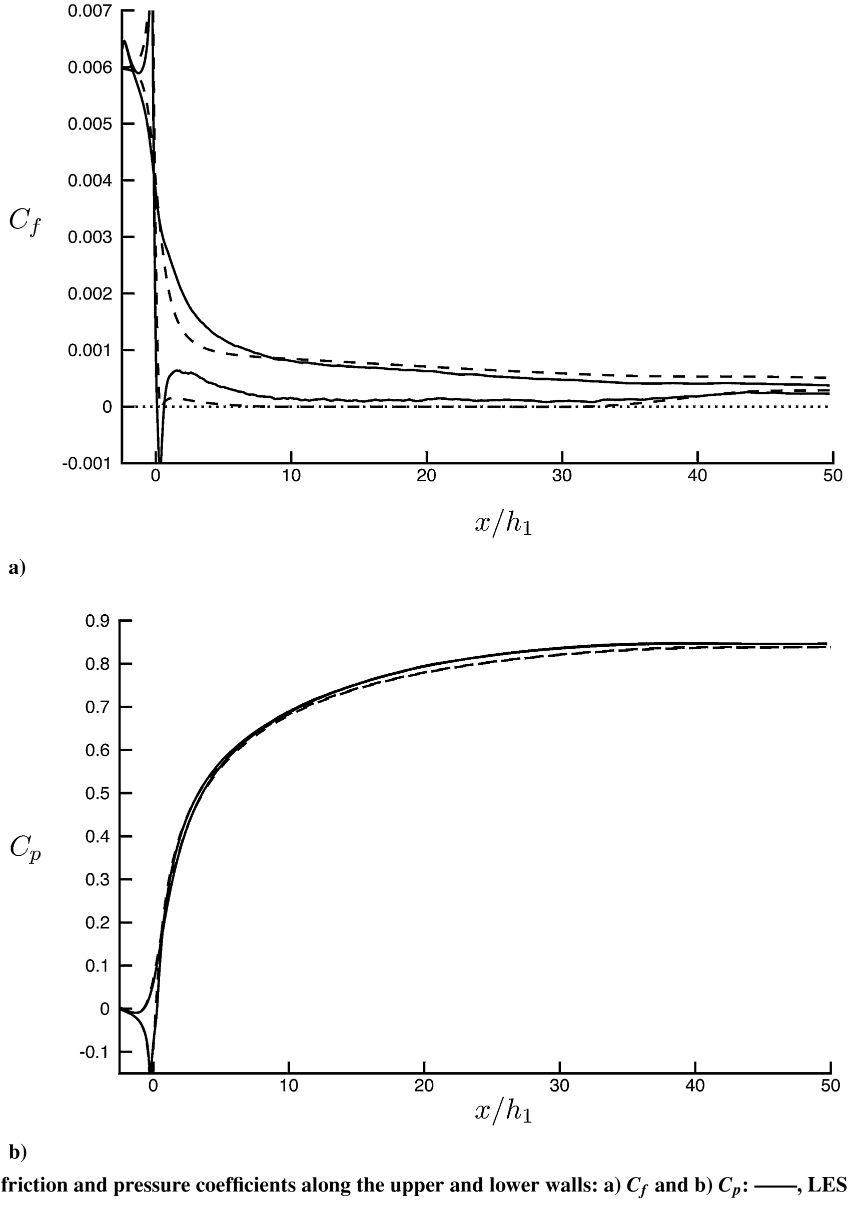

Fig. 14 Skin-friction and pressure coefficients along the upper and lower walls: a) C_f and b) C_p: ——, LES and – – –, V2F.

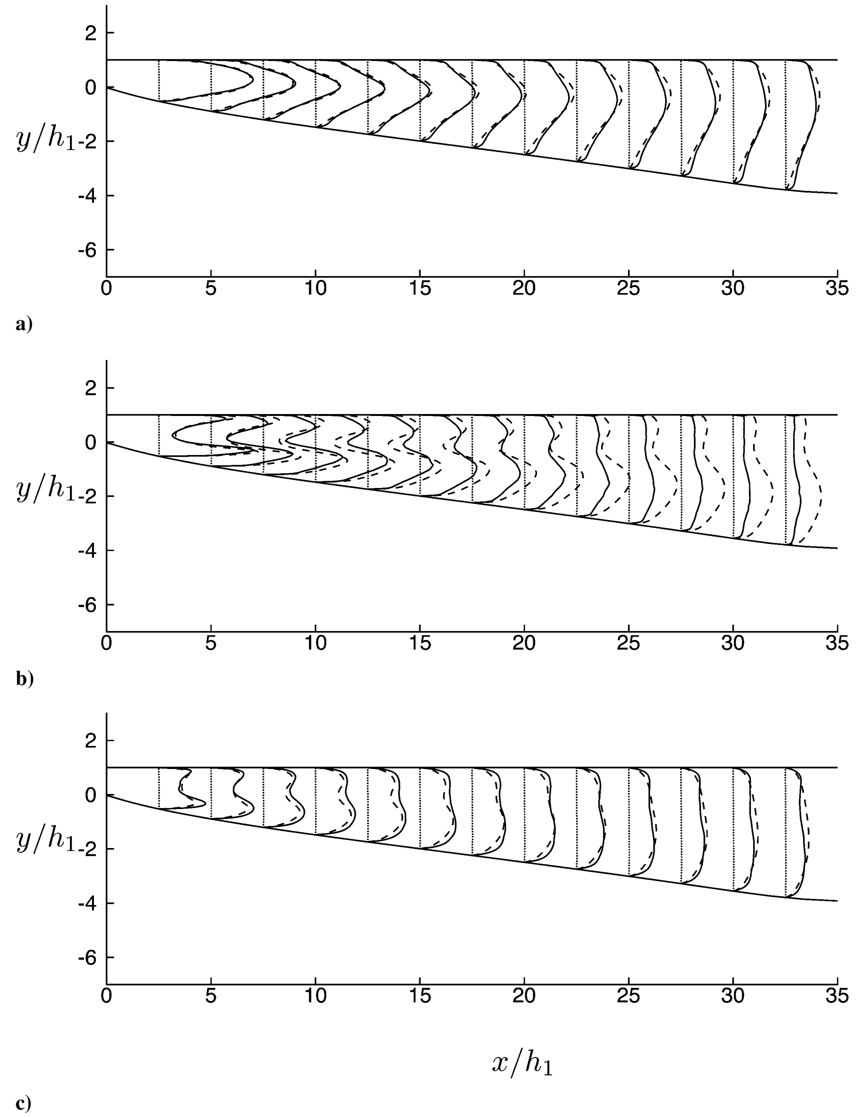

Fig. 15 Profiles of mean velocity $\bar{u}$, turbulent kinetic energy k, and wall-normal velocity fluctuations $\overline{v'^2}$: a) mean velocity, $x/h_1 + 5 \times \bar{u}/u_b$; b) turbulent kinetic energy, $x/h_1 + 250 \times k/u_b^2$; and c) wall-normal velocity fluctuations, $x/h_1 + 25 \times \overline{v'^2}/u_b^2$: ——, LES and – – –, V2F.

The computational time step is fixed to be $\Delta t = 0.02 h_1/u_b$. After the flow inside the diffuser reaches statistically steady state, the turbulence statistics are obtained by averaging over 24,000 time steps, during which the flow goes through the diffuser approximately four times. From the assumption of the homogeneity in the spanwise direction, spanwise averaging is conducted simultaneously.

B. Results

Figure 14 shows the distributions of the skin-friction and pressure coefficients along the upper and lower walls of the optimal diffuser by LES and V2F. As shown, the pressure coefficients from LES and V2F are in an excellent agreement, whereas the skin friction coefficients are in reasonable agreement. With LES, the skin friction in the shape design region is slightly higher than zero, but it is still very small compared to that of the flat-plate boundary-layer flow. Also note from the LES result that there exists a small separation region ($x/h_1 = 0 \sim 1$) around the diffuser throat, which is not observed from the V2F result. This is similar to the finding by Kaltenbach et al.[41] that the result from LES shows a small separation region near the diffuser throat for the initial diffuser shape, whereas the separation region does not exist from the V2F result. Because the optimal shape expands more rapidly near the diffuser throat than the initial shape (Fig. 9), a larger separation occurs near the throat of the optimal diffuser. From this comparison, the V2F model seems to produce a bit of a too rapid expansion around the diffuser throat because the turbulence model cannot accurately predict the flow around the corner with rapid expansion. However, this geometric variation near the throat has little effect on the whole performance of the optimal diffuser (Fig. 14b).

Figure 15 shows the profiles of the mean velocity $\bar{u}$, turbulent kinetic energy k, and wall-normal velocity fluctuations $\overline{v'^2}$ at several x locations. The profiles of the mean velocity and wall-normal velocity fluctuations from LES agree with those from V2F. The profiles of turbulent kinetic energy are in good agreement in the upstream part of the diffuser and begin to deviate from each other at about $x/h_1 = 20$. The same discrepancy in k was also found in the downstream region of the initial diffuser when we compared the results from LES by Kaltenbach et al.[41] and V2F.

Figure 16 shows the reverse flow factor γ along the optimal diffuser walls. The reverse flow factor is obtained as the fraction of time of flow reversal to the total time, and the time- and spanwise-averaged values are plotted in Fig. 16. From Fig. 16, the reverse flow factor on the lower wall increases up to 70% in the small mean separation region around $x = 0$, and this factor suddenly falls off down to 40%. The reverse flow factor is $30 \sim 40\%$ in most of the shape design region and gradually decreases to zero. In general, the reverse flow factor γ is 50% at the point where the mean skin friction is zero. (Also see Na and Moin.[50]) Because the mean skin friction from LES is not exactly zero but slightly positive along the lower wall, the reverse flow factor in this region is below

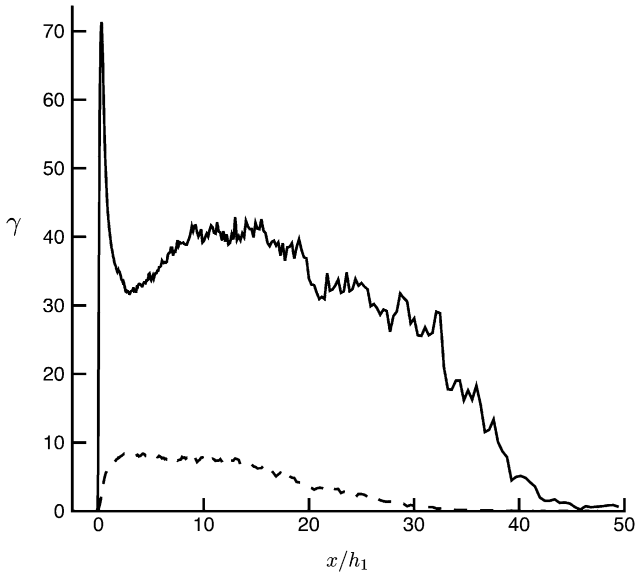

Fig. 16 Distribution of reverse flow factor along the walls: ——, lower wall and – – –, upper wall.

50%. On the upper wall, where the mean skin friction is relatively high, $\gamma \leq 10\%$, indicating that the reverse flow occurs along the upper wall even far downstream of the entrance, although γ is very small.

Figure 17 shows the contours of the instantaneous skin friction on the upper and lower walls, where the white regions represent the negative skin friction and darker regions represent higher skin friction. In the inlet channel region of $-2.5 < x/h_1 < 0$, streaky structures are clearly observed on both the upper and lower walls. On the upper wall, these streaks are much attenuated after the diffuser throat, $x = 0$, but are still observed at a downstream region. On the lower wall, these streaks suddenly disappear at the diffuser throat, $x = 0$, where patches of reverse flow appear. These patches of reverse flow are broken by high-momentum fluids penetrating into the wall. (Dark spots are observed at $0 < x/h_1 < 5$.) Large patches of reverse flow are formed at a downstream region and disappear farther downstream where the skin friction becomes larger.

Figure 18 shows the time histories of the skin-friction coefficient on the lower wall at a few x locations. At $x/h_1 = 0.5$, which locates in the mean flow separation region, negative skin frictions fluctuate apparently at high frequencies. As the flow goes downstream, the timescale of the skin friction fluctuations becomes larger.

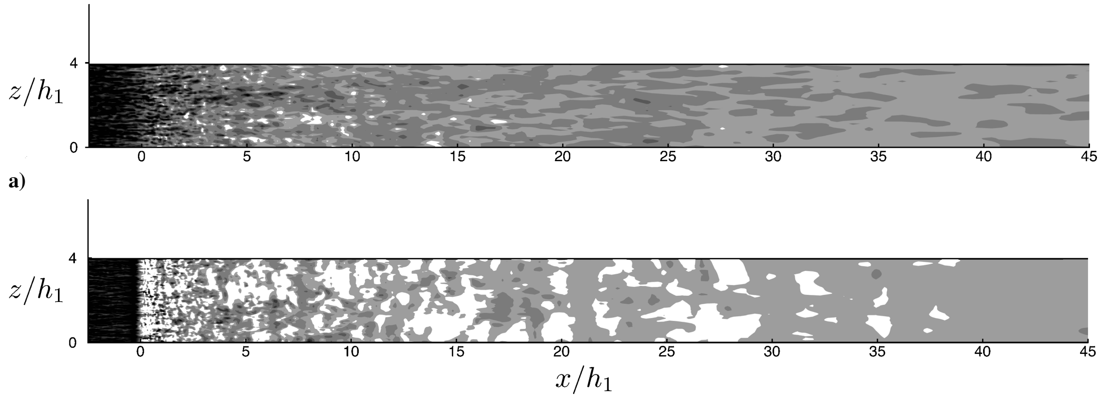

a)

b)

Fig. 17 Contours of the instantaneous skin friction (where white regions represent reverse flow): a) upper wall and b) lower wall.

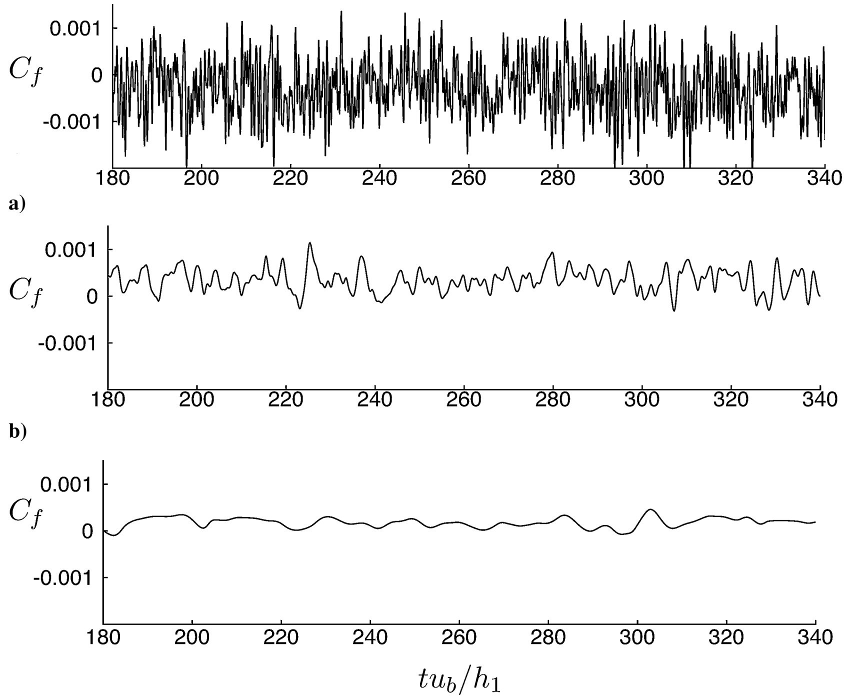

a)

b)

c)

Fig. 18 Time histories of skin-friction coefficient on lower wall at various x locations: a) $x/h_1 = 0.5$, b) $x/h_1 = 5$, and c) $x/h_1 = 20$.

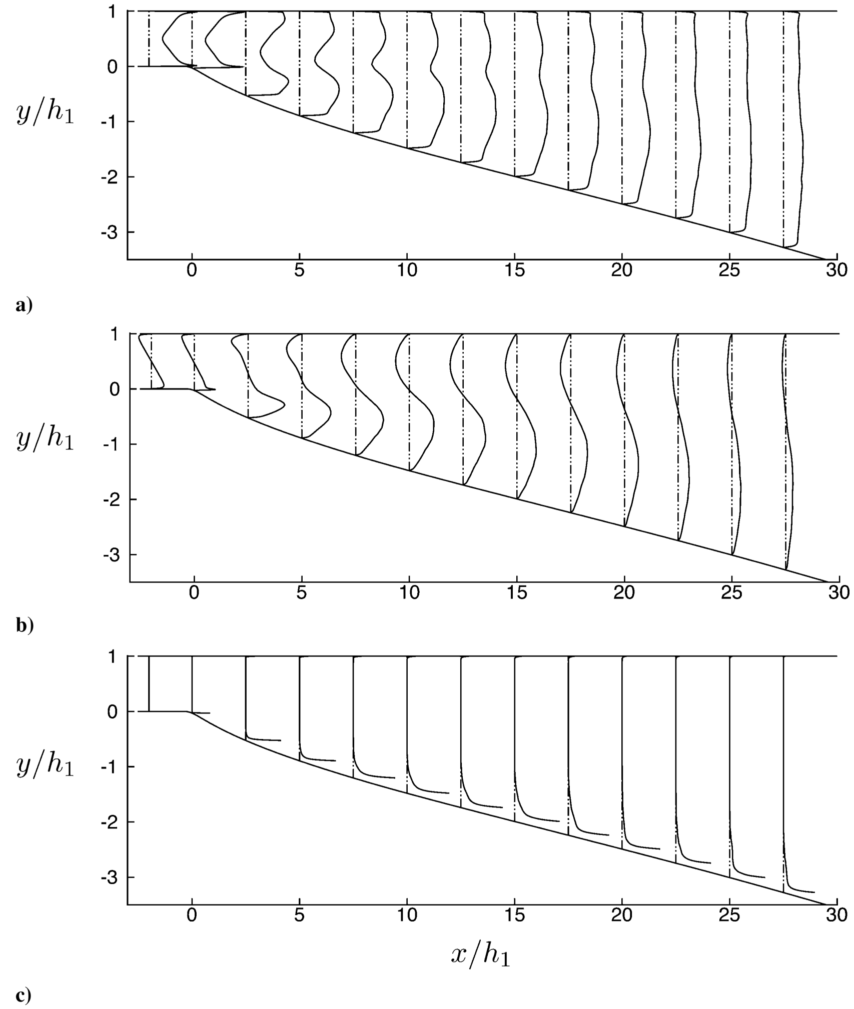

Fig. 19 RMS streamwise velocity fluctuations, Reynolds shear stress and reverse flow factor: a) $x/h_1 + 15 \times u_{\mathrm{rms}}/u_b$, b) $x/h_1 - 250 \times u'v'/(u_b^2)$, and c) $x/h_1 + 5 \times \gamma$.

Figure 19 shows the profiles of the Reynolds stresses and reverse flow factor at various x locations. The turbulence intensity rapidly increases as the flow enters the diffuser. The point where the turbulence intensity has maximum values is near the wall in the inlet channel region and moves away from the wall farther downstream. The Reynolds shear stress shows the same tendency. The reverse flow factor has maximum value at the wall and rapidly decreases to zero from the wall. Note also that the onset point of the instantaneous back flow, $\gamma > 0$, moves away from the wall as the flow goes downstream.

VI. Effect of the Turbulence Model

In Sec. IV, we showed the results of the optimal shape design using the V2F model, and one of the results was confirmed by a separate LES in Sec. V. It is clear from those sections that, for the accurate shape design of a diffuser, a turbulence model should accurately predict the flow with separation and the flow above the zero skin friction wall.

Algebraic turbulence models or zero-equation models such as the Baldwin–Lomax model[51] are still widely used especially in the design of airfoil shape due to their simplicity.[33,35] However, those models demonstrate poor prediction for flow with strong adverse pressure gradient and separation, and also they are not adequate for the simulation of complex internal flow due to the ambiguity in determining the outer-layer eddy viscosity. Therefore, in this study, we test two popular two-equation turbulence models: low Reynolds number k–ϵ model by Launder–Sharma[52] (L–S) and k–ω shear stress transport (SST) model by Menter.[53] The standard high-Reynolds-number k–ϵ model is not considered here because the wall boundary condition is based on the wall function that is not appropriate for simulation of flow with zero or negative skin friction during optimization. Therefore, in the present section, we test the L–S and SST models for the initial diffuser and the optimal diffuser of case 5. The details about these turbulence models and their constants are given in Refs. 52 and 53.

Figure 20 shows the distributions of the skin-friction and pressure coefficients along the lower and upper walls of the initial diffuser with different turbulence models, together with those from LES.[41] As shown, with the L–S model, the skin friction is positive along the lower wall and the pressure is overpredicted as compared to those with other turbulence models, indicating that the L–S model fails to predict the mild flow separation on the lower wall. On the other hand, the SST and V2F models successfully predict the flow inside the initial diffuser, although flow separation occurs at an earlier location with SST as compared to those with V2F and LES.

Figure 21 shows the distributions of the skin-friction and pressure coefficients along the lower and upper walls of the optimal diffuser for case 5 with different turbulence models, together with those from the present LES. Again, the L–S model does not predict the flow inside the optimal diffuser. With the SST model, a relatively large negative skin-friction region exists in $0 < x/h_1 < 10$. Because of this negative skin friction, the pressure does not quickly recover, which results in a slightly lower pressure recovery at the diffuser exit than those from V2F and LES. However, the zero skin friction is indeed obtained in most of the design region, which suggests that the SST model may be one of the possible candidates for the accurate design of a diffuser in turbulent flow.

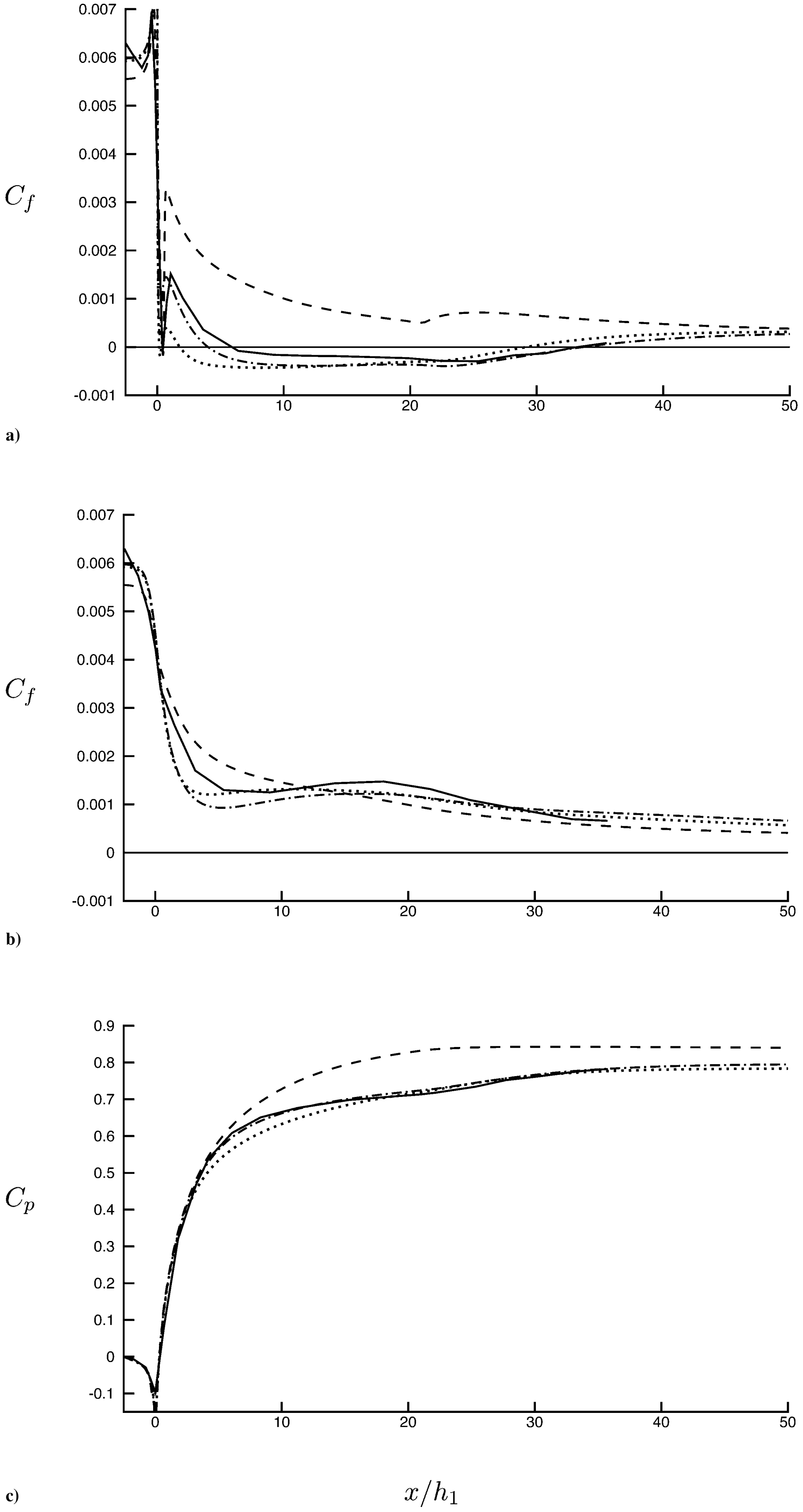

Fig. 20 **Skin-friction and pressure distributions for the initial diffuser: a) C_f along the lower wall, b) C_f along the upper wall, and c) C_p along the lower wall: ‒‒‒, L–S; · · · ·, SST; ‒·‒·‒, V2F; and ——, LES.[41]**

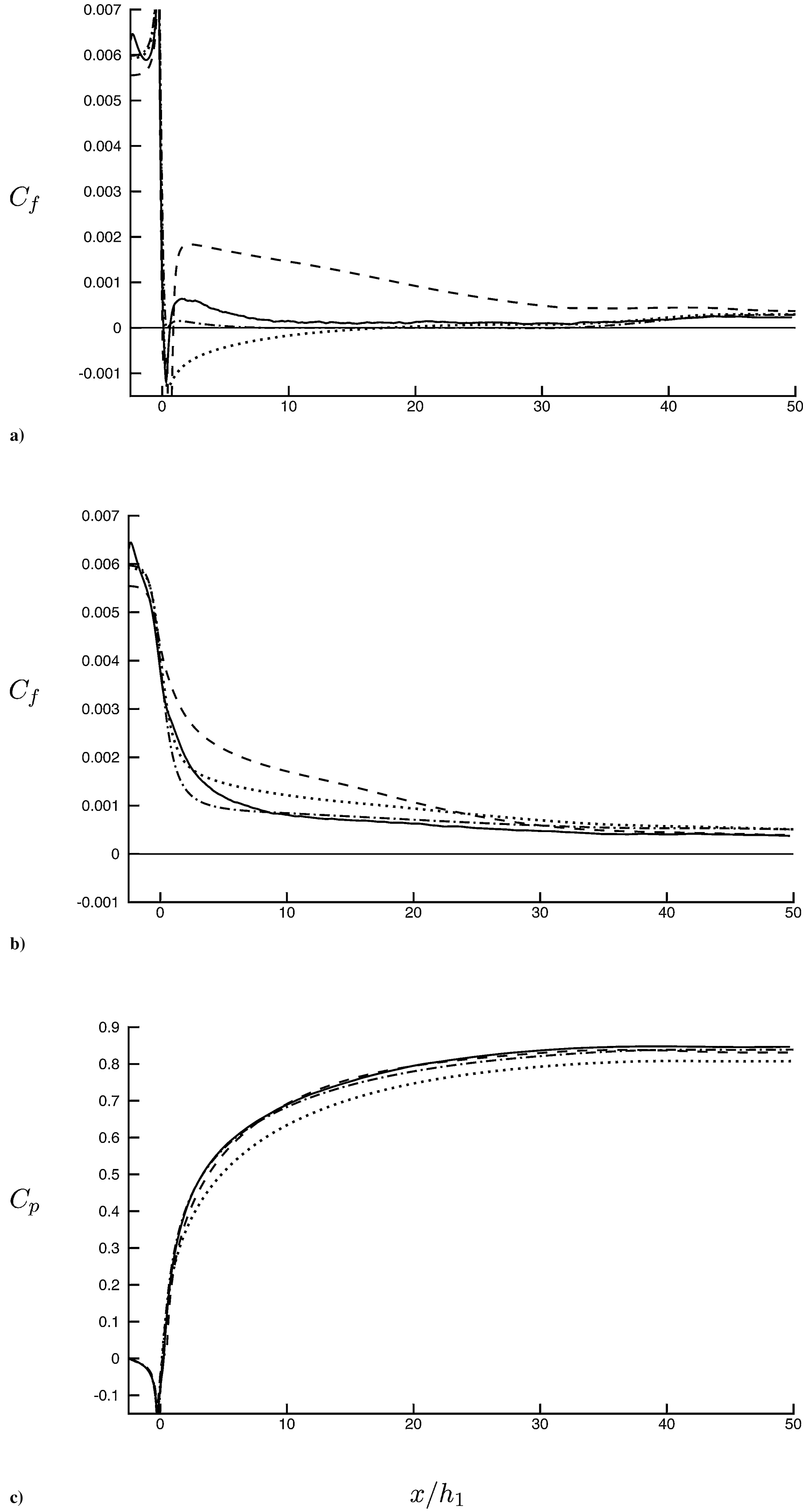

Fig. 21 **Skin-friction and pressure distributions for the optimal diffuser of case 5: a) C_f along the lower wall, b) C_f along the upper wall, and c) C_p along the lower wall: – – –, L–S; · · · ·, SST; –·–·–, V2F; and ——, LES.**

VII. Summary

In this study, we designed the optimal shape of a two-dimensional asymmetric diffuser with maximum pressure recovery at the exit in turbulent flow, by use of a mathematical theory based on the variational calculus and gradient algorithm. The optimality condition for maximum pressure recovery was obtained to be zero skin friction along the diffuser wall, and optimal shapes were obtained through iterative procedures to satisfy the optimality condition. We used the k–ϵ–v^2–f (V2F) model for flow simulation. The initial diffuser shape was set to be a two-dimensional asymmetric diffuser for which much experimental and numerical data are available. This initial diffuser, with mild flow separation, has been a challenging test problem for turbulence model, and Durbin[38] successfully tested his V2F model in simulation of the flow inside this initial shape. Therefore, from this initial shape, we designed the optimal shapes for six different geometric constraints (cases 1–6).

In the optimal shape obtained, the skin friction was indeed nearly zero in the shape design region, and flow separation that appeared in the initial shape was completely removed or significantly reduced. In all six cases, the upstream parts of the optimal diffusers were nearly identical irrespective of different geometric constraints. In the optimal diffuser, about $5 \sim 10\%$ increase in the pressure recovery was achieved, and the diffuser effectiveness was improved. The total pressure loss was also much reduced as compared to the initial diffuser.

LES was performed for the optimal diffuser shape of case 5 to confirm the shape design result. The skin friction on the shape design area from LES was slightly higher than zero, but was still very small as compared to that of the flat-plate boundary-layer flow. The skin friction, wall pressure, mean velocity, and turbulence quantities from LES were in reasonably good agreement with those from the k–ϵ–v^2–f turbulence model.

The present approach using an adjoint-based gradient algorithm together with the V2F model is quite useful for the shape optimization in turbulent flow, although it may have some inherent limitations such as the complexity of the derivation of the optimality condition according to the choice of the cost function, the possible dependence on the initial condition, and the shortcoming of the turbulence model. Our study was focused on the investigation of the accuracy of the shape design results and the adequacy of turbulence model for flow simulation in the optimization procedure. Specifically, from an LES, we confirmed that the V2F model predicts the flow characteristics inside the optimal diffuser very well, where the skin friction is zero along the diffuser wall. This confirmation test and the performance tests of other turbulence models conducted in this study suggest that a turbulence model predicting flow separation accurately is a key element in the optimal shape design of flow systems containing separation.

Acknowledgment

This work was supported by the Creative Research Initiatives of the Korean Ministry of Science and Technology.

References

[1] Kline, S. J., Abbott, D. E., and Fox, R. W., "Optimum Design of Straight-Walled Diffusers," *Journal of Basic Engineering*, Vol. 81, 1959, pp. 321–331.

[2] Waitman, B. A., Reneau, L. R., and Kline, S. J., "Effects of Inlet Conditions on Performance of Two-Dimensional Subsonic Diffusers," *Journal of Basic Engineering*, Vol. 83, 1961, pp. 349–360.

[3] Fox, R. W., and Kline, S. J., "Flow Regimes in Curved Subsonic Diffusers," *Journal of Basic Engineering*, Vol. 84, 1962, pp. 303–316.

[4] Reneau, L. R., Johnston, J. P., and Kline, S. J., "Performance and Design of Straight, Two-Dimensional Diffusers," *Journal of Basic Engineering*, Vol. 89, 1967, pp. 141–150.

[5] Stratford, B. S., "Prediction of Separation of the Turbulent Boundary Layer," *Journal of Fluid Mechanics*, Vol. 5, 1959, pp. 1–16.

[6] Stratford, B. S., "An Experimental Flow with Zero Skin Friction Throughout Its Region of Pressure Rise," *Journal of Fluid Mechanics*, Vol. 5, 1959, pp. 17–35.

[7] Townsend, A. A., "The Development of Turbulent Boundary Layers with Negligible Wall Stress," *Journal of Fluid Mechanics*, Vol. 8, 1960, pp. 143–155.

[8] Townsend, A. A., "Self-Preserving Development Within Turbulent Boundary Layers in Strong Adverse Pressure Gradients," *Journal of Fluid Mechanics*, Vol. 23, 1965, pp. 767–778.

[9] Dengel, P., and Fernholz, H. H., "An Experimental Investigation of an Incompressible Turbulent Boundary Layer in the Vicinity of Separation," *Journal of Fluid Mechanics*, Vol. 212, 1990, pp. 615–636.

[10] Rakesh, K. S., and Ram, S. A., "Structure of Turbulence in an Incipient-Separating Axisymmetric Flow," *Journal of Fluids Engineering*, Vol. 117, 1995, pp. 433–438.

[11] Elsberry, K., Loeffler, J., Zhou, M. D., and Wygnanski, I., "An Experimental Study of a Boundary Layer That Is Maintained on the Verge of Separation," *Journal of Fluid Mechanics*, Vol. 423, 2000, pp. 227–261.

[12] Hammache, M., Browand, F. K., and Blackwelder, R. F., "Whole-Field Velocity Measurements Around an Axisymmetric Body with a Stratford–Smith Pressure Recovery," *Journal of Fluid Mechanics*, Vol. 461, 2002, pp. 1–24.

[13] Carlson, J. J., Johnston, J. P., and Sagi, C. J., "Effects of Wall Shape on Flow Regimes and Performance in Straight, Two-Dimensional Diffusers," *Journal of Basic Engineering*, Vol. 89, 1967, pp. 151–160.

[14] Strawn, R. C., and Kline, S. J., "A Stall Margin Design Method for Planar and Axisymmetric Diffusers," *Journal of Fluids Engineering*, Vol. 105, 1983, pp. 28–33.

[15] Ghose, S., and Kline, S. J., "The Computation of Optimum Pressure Recovery in Two-Dimensional Diffusers," *Journal of Fluids Engineering*, Vol. 100, 1978, pp. 419–426.

[16] Bardina, J., Lyrio, A., Kline, S. J., Ferziger, J. H., and Johnston, J. P., "A Prediction Method for Planar Diffuser Flows," *Journal of Fluids Engineering*, Vol. 103, 1981, pp. 315–321.

[17] Pironneau, O., "On Optimum Profiles in Stokes Flow," *Journal of Fluid Mechanics*, Vol. 59, 1973, pp. 117–128.

[18] Pironneau, O., "On Optimum Design in Fluid Mechanics," *Journal of Fluid Mechanics*, Vol. 64, 1974, pp. 97–110.

[19] Glowinski, R., and Pironneau, O., "On the Numerical Computation of the Minimum-Drag Profile in Laminar Flow," *Journal of Fluid Mechanics*, Vol. 72, 1975, pp. 385–389.

[20] Baysal, O., and Eleshaky, M. E., "Aerodynamic Design Optimization Using Sensitivity Analysis and Computational Fluid Dynamics," *AIAA Journal*, Vol. 30, No. 3, 1992, pp. 718–725.

[21] Eleshaky, M. E., and Baysal, O., "Airfoil Shape Optimization Using Sensitivity Analysis on Viscous Flow Equations," *Journal of Fluids Engineering*, Vol. 115, 1993, pp. 75–84.

[22] Anderson, W. K., Newman, J. C., Whitfield, D. L., and Nielsen, E. J., "Sensitivity Analysis for Navier–Stokes Equations on Unstructured Meshes Using Complex Variables," *AIAA Journal*, Vol. 39, No. 1, 2001, pp. 56–63.

[23] Cabuk, H., and Modi, V., "Optimum Plane Diffusers in Laminar Flow," *Journal of Fluid Mechanics*, Vol. 237, 1992, pp. 373–393.

[24] Ganesh, R. K., "The Minimum Drag Profile in Laminar Flow: A Numerical Way," *Journal of Fluids Engineering*, Vol. 116, 1994, pp. 456–462.

[25] Kuruvila, G., Ta'asan, S., and Salas, M. D., "Airfoil Design and Optimization by the One-Shot Method," AIAA Paper 95-0478. Jan. 1995.

[26] Jameson, A., Martinelli, L., and Pierce, N. A., "Optimum Aerodynamic Design Using the Navier–Stokes Equations," *Theoretical and Computational Fluid Dynamics*, Vol. 10, 1998, pp. 213–237.

[27] Nielsen, E. J., and Anderson, W. K., "Aerodynamic Design Optimization on Unstructured Meshes Using the Navier–Stokes Equations," *AIAA Journal*, Vol. 37, No. 11, 1999, pp. 1411–1419.

[28] Vicini, A., and Quagliarella, D., "Inverse and Direct Airfoil Design Using a Multiobjective Genetic Algorithm," *AIAA Journal*, Vol. 35, No. 9, 1997, pp. 1499–1505.

[29] Vicini, A., and Quagliarella, D., "Airfoil and Wing Design Through Hybrid Optimization Strategies," *AIAA Journal*, Vol. 37, No. 5, 1999, pp. 634–641.

[30] Madsen, J. I., Shyy, W., and Haftka, R. T., "Response Surface Techniques for Diffuser Shape Optimization," *AIAA Journal*, Vol. 38, No. 9, 2000, pp. 1512–1518.

[31] Wang, X., and Damodaran, M., "Aerodynamic Shape Optimization Using Computational Fluid Dynamics and Parallel Simulated Annealing Algorithms," *AIAA Journal*, Vol. 39, No. 8, 2001, pp. 1500–1508.

[32] Zhang, J., Chu, C. K., and Modi, V., "Design of Plane Diffusers in Turbulent Flow," *Inverse Problems in Engineering*, Vol. 2, 1995, pp. 85–102.

[33] Soemarwoto, B., "The Variational Method for Aerodynamic Optimization Using the Navier–Stokes Equations," ICASE Rept. 97-71, Dec. 1997.

[34] Mohammadi, B., "A New Optimal Shape Design Procedure for Inviscid and Viscous Turbulent Flows," *International Journal for Numerical Methods in Fluids*, Vol. 25, 1997, pp. 183–203.

[35] Kim, S., Alonso, J., and Jameson, A., "A Gradient Accuracy Study for the Adjoint-Based Navier–Stokes Design Method," AIAA Paper 99-0299, Jan. 1999.

[36] Anderson, W. K., and Bonhaus, D. L., "Airfoil Design on Unstructured Grids for Turbulent Flows," *AIAA Journal*, Vol. 37, No. 2, 1999, pp. 185–191.

[37] Durbin, P., "Near-Wall Turbulence Closure Modeling Without Damping Functions," *Theoretical and Computational Fluid Dynamics*, Vol. 3, 1991, pp. 1–13.

[38] Durbin, P., "Separated Flow Computations with the k–e–$v2$ Model," *AIAA Journal*, Vol. 33, No. 4, 1995, pp. 659–664.

[39] Obi, S., Aoki, K., and Masuda, S., "Experimental and Computational Study of Turbulent Separating Flow in an Asymmetric Plane Diffuser," *9th Symposium on Turbulent Shear Flows*, Kyoto, Japan, 1993, pp. P305-1–P305-4.

[40] Buice, C. U., and Eaton, J. K., "Experimental Investigation of Flow Through an Asymmetric Plane Diffuser," *Annual Research Briefs—1996*, Center for Turbulence Research, Stanford Univ./NASA Ames Research Center, 1996, pp. 243–248.

[41] Kaltenbach, H.-J., Fatica, M., Mittal, R., Lund, T. S., and Moin, P., "Study of Flow in a Planar Asymmetric Diffuser Using Large-Eddy Simulation," *Journal of Fluid Mechanics*, Vol. 390, 1999, pp. 151–185.

[42] Kim, C. S., Kim, C., and Rho, O. H., "Sensitivity Analysis for the Navier–Stokes Equations with Two-Equation Turbulence Models," *AIAA Journal*, Vol. 39, No. 5, 2001, pp. 838–845.

[43] Leonard, B. P., "A Stable and Accurate Convective Modelling Procedure Based on Quadratic Upstream Interpolation," *Computer Methods in Applied Mechanics and Engineering*, Vol. 19, 1979, pp. 59–98.

[44] Patankar, S. V., *Numerical Heat Transfer and Fluid Flow*, McGraw–Hill, New York, 1980, Chap. 6.

[45] Japikse, D., and Baines, N. C., *Diffuser Design Technology*, Concept ETI, Norwich, VT, 1998, Chap. 2.

[46] Runstadler, P. W., Jr., and Dolan, F. X., "Further Data on the Pressure Recovery of Straight-Channel, Plane-Divergence Diffusers at High Subsonic Mach Numbers," *Journal of Fluids Engineering*, Vol. 95, 1973, pp. 373–384.

[47] Germano, M., Piomelli U., Moin, P., and Cabot, W. H., "A Dynamic Subgrid-Scale Eddy-Viscosity Model," *Physics of Fluids A*, Vol. 3, 1991, pp. 1760–1765.

[48] Lilly, D. K., "A Proposed Modification of the Germano Subgrid Scale Closure Method," *Physics of Fluids A*, Vol. 3, 1992, pp. 2746–2757.

[49] Lund T. S., "On the Use of Discrete Filters for Large Eddy Simulation," *Annual Research Briefs—1997*, Center for Turbulence Research, Stanford Univ./NASA Ames Research Center, 1997, pp. 83–95.

[50] Na, Y., and Moin, P., "Direct Numerical Simulation of a Separated Turbulent Boundary Layer," *Journal of Fluid Mechanics*, Vol. 374, 1998, pp. 379–405.

[51] Baldwin, B. S., and Lomax, H., "Thin-Layer Approximation and Algebraic Model for Separated Turbulent Flows," AIAA Paper 78-257, Jan. 1978.

[52] Launder, B. E., and Sharma, B. I., "Application of the Energy-Dissipation Model of Turbulence to the Calculation of Flow near a Spinning Disc," *Letters in Heat and Mass Transfer*, Vol. 1, 1974, pp. 131–138.

[53] Menter, F. R., "Two-Equation Eddy-Viscosity Turbulence Models for Engineering Applications," *AIAA Journal*, Vol. 32, No. 8, 1994, pp. 1598–1605.

A. Plotkin
Associate Editor